

A NUMERICAL INVESTIGATION OF FLOWS OF SHEAR-THINNING FLUIDS WITH APPLICATIONS TO BLOOD RHEOLOGY

JAROSLAV HRON, JOSEF MÁLEK, AND STEFAN TUREK

ABSTRACT. We provide a new solver for the flow of power-law fluids that extends a solver developed by S. Turek (see [18]) for the Navier-Stokes fluid. This solver is convenient to simulate efficiently both steady and unsteady flows of shear-dependent fluids in a complex geometry. To illustrate the ability of the solver, two specific problems were chosen. First, we study steady flows of power-law fluids in corrugated channels, and carry out qualitative comparisons with real experiments. The attention is paid to the dependences of friction factor and dimensionless normal stress amplitude on the aspect ratio (amplitude versus wavelength of the sinusoidal channel) and to the occurrence of secondary flows. We show that the aspect ratio is not a sensible non-dimensional number in this geometry. Secondly, we simulate unsteady (pulsatile) flows of the power-law fluid (i.e. blood under certain circumstances) in the presence of stenosis and we obtain a very good coincidence with recent numerical studies. The description of numerical scheme and theoretical background are also outlined.

1. INTRODUCTION

There are many engineering problems which lead to the investigation of the flow of both Newtonian and non-Newtonian fluids in complex geometry. To be more specific, we can name the area of biomechanical engineering studying blood flow in arteries and other blood vessels or the area of chemical and process engineering studying flows in porous media. Periodically constricted tubes or channels with corrugated walls are used to model the converging and diverging nature of porous media or blood vessels. In all these cases, we can observe a periodic constriction of the flow channel or a periodic change of the flow direction. The simplest model for such geometry used in many experiments and simulations is a periodically constricted tube or in two dimensions a channel with corrugated walls (see Figure 1).

Shear-dependent fluids, as a significant class of non-Newtonian models, are defined by a polynomial dependence of the (generalized) viscosity on the modulus of the symmetric velocity gradient. If this viscosity function is increasing, the corresponding fluids are called shear thickening, while fluids, where the viscosity decreases for increasing shear rate are named shear thinning fluids. The latter has broad applications in engineering practice; we can find them in chemical engineering (cf. [16]), geology (cf. [2, 12]), blood rheology (see [23]), glaciology (cf. [8]), it can also be used to model boundary layer type of behavior (see [13, 14]).

This research was supported by the Grant Agency of the Czech Republic, grant No. 201/96/0228 and by CEZ:J13/9811320007.

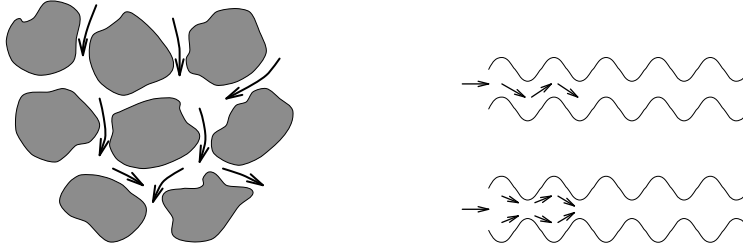


FIGURE 1. Flow in porous media and model flow in corrugated channels

The objective of the first two paragraphs is to recall that there is a large number of engineering problems that require better understanding of flows of non-Newtonian (in particular power-law) fluids in a real (i.e. complex) geometry. These are the areas, where numerical simulations produced by an effective solver can help significantly.

Thus, the aim of this paper is to present a numerical code that would be competitive to study adequately various complex flows from engineering applications mentioned above. For the Navier-Stokes equations such a solver has been developed by Stefan Turek, see [18]. The main advantages of this code are

- simple and stable spatial discretization by \tilde{Q}_1/Q_0 nonconforming finite elements on quadrilateral meshes
- adaptive stabilization techniques for the convective term (upwinding or streamline diffusion)
- Multilevel Pressure Schur Complement techniques for treating the saddle point problems
- fast and robust multigrid solver for linear problems
- adaptive fixed-point defect correction schemes for nonlinear parts
- fractional step θ -scheme for time discretization with adaptive selection of the time step for the nonstationary flows

The solver makes it possible to consider non-linear models for stress.

We show in this paper that such solver can be extended (modified) to be applicable also to the various kinds of fluids with non-constant (shear-dependent) viscosity. For the numerical experiments, we consider only the power-law types of viscosity functions. However, we wish to underline that we can include an arbitrary form of the viscosity function into the code without having any significant growth of computational effort, and in fact, this enlargement of the code is a recent project (see also <http://www.featflow.de>).

For this presentation, we choose two problems, one for steady, the second for unsteady motions. Both problems can be viewed as a first attempt in understanding of blood flows, as explained later.

The first problem deals with flows in corrugated channels (see Fig. 1). This has been motivated by an experimental investigation of R. C. Yalamanchili [21, 22] where the experiments in channels with corrugated walls were performed for the fluid consisting of 60% water, 40% glycerine with added 0ppm, 500ppm or 2000ppm polyacrylamide. Such a fluid exhibits non-zero normal stress differences but has constant viscosity in range of shear-rate they measured. It means that the material is a viscoelastic, non shear-thinning fluid. Therefore, we can verify our

numerical simulations with the measured experimental data only qualitatively. We have found (see section 3) very good correspondence between the numerical results and experimental data from [21], that are caused by the geometry of the domain. It mainly concerns the structure of the velocity field, the location of maximum velocity amplitude, the length of acceleration zone, eddies forming secondary flows, etc. For the experiments a channel with two sinusoidal plates was used. Then, it is reasonable to consider two dimensional domain for numerical simulations. In coincidence with [21], we have also observed that aspect ratio¹ $\frac{a}{\lambda}$, where a is the amplitude and λ is the wavelength of the channel oscillations, cannot be used as a good measure even for power-law fluids; for two different channels with the same aspect ratio we have observed differences in the structure of corresponding flows, see Fig. 8.

The second problem, analyzed here, deals with the pulsatile flow in channels with stenosis, and we compare our results with those presented in [17], where detail comparison with previous experimental and numerical studies is discussed, and where also the importance of such numerical simulations is clarified.

We wish to recall that the simulation of blood flow in a cardiovascular system is challenging, clearly very important, and not yet satisfactorily answered problem, which is because of many properties of blood that need to be considered, and makes the modeling of blood flow very complicated. From the basic features we can name:

1. 3D flow in complex geometry
2. complex rheological behavior of blood
3. pulsativity of the flow and consequently pulsativity of the walls
4. inelastic permeable walls
5. different deformability of the red cells at different shear rates, etc.

From this point of view, our numerical experiments can be considered as one of the preliminary steps in simulating blood flow. However, there are just few calculations involving a complicated geometry and nonlinear fluid, thus this paper aims to focus on this lacunae.

In the next section we describe the analyzed model, completed by boundary conditions and the constitutive formulae for the viscous part of the stress tensor. We also present, in brief, known theoretical results concerning the existence of weak solution and its uniqueness and regularity, and give a description of used numerical scheme for the Navier-Stokes equations. A big advantage of this scheme is its “easy” modification for shear-dependent fluids which is presented here for the first time. Section 3 contains numerical results, their comparison and analysis for the flows in corrugated channels, while section 4 is devoted to pulsatile flows in channels with stenosis. Conclusions form the final part of the paper.

2. EQUATIONS AND NUMERICAL METHODS

We consider both, steady and unsteady motions of an incompressible fluid in a two-dimensional domain Ω . Such a flow is governed by the following equations

$$(2.1) \quad \operatorname{div} \vec{v} = 0,$$

$$(2.2) \quad \varrho \left(\frac{\partial \vec{v}}{\partial t} + \sum_{j=1}^2 v_j \frac{\partial \vec{v}}{\partial x_j} \right) = -\operatorname{grad} p + \operatorname{div} \mathbf{T}^E + \varrho \vec{f},$$

¹Here, the *aspect ratio* has different meaning than in FEM or multigrid where it is the quotient between (local) length and width of quadrilaterals which is essential for the numerical behavior.

where $\vec{v} = (v_1, v_2)$ is the velocity vector, ρ is the constant density of the fluid, p is the pressure field, $\vec{f} = (f_1, f_2)$ is the field of body forces per mass unit and \mathbf{T}^E is the viscous part of the stress tensor.

We deal with a viscous fluid, which is modeled by²

$$(2.3) \quad \mathbf{T}^E = 2\mu(|\mathbf{D}|^2)\mathbf{D},$$

where $\mathbf{D} = \frac{1}{2}(\nabla\vec{v} + (\nabla\vec{v})^T)$ is the symmetric part of the velocity gradient. Since the modulus of \mathbf{D} corresponds in viscometric flows to shear rate, the fluids undergoing (2.3) are called the fluids with shear-dependent viscosity. Numerical tests were performed for the simple power-law model with two parameters ε and α in the form

$$(2.4) \quad \mu(|\mathbf{D}|^2) = 2\mu_0 (\varepsilon + |\mathbf{D}|)^{-\alpha},$$

where $\varepsilon > 0$, $\alpha \in [0, 1]$ and μ_0 is given viscosity constant. Tests were made for $\vec{f} = 0$ and the value $\frac{\mu_0}{\rho} = 0.042 \text{ cm}^{-2} \text{ s}^{-1}$ and $\vec{f} = 0$. The Reynolds number $\text{Re} = \frac{V_0 L \rho}{\mu_0}$ is based on the channel width L and on the maximum of the inflow velocity V_0 . In the sequel we use the non-dimensionalized form of equations (2.2) with the viscosity ν defined by $\nu = \frac{\mu}{\rho V_0 L}$.

For the sake of completeness, we briefly describe in this section the numerical methods used in Featflow code, together with the modifications of this solver needed to include nonlinear viscous (explicitly given) function $\mu(|\mathbf{D}|^2)$ into the program. Some other numerical approaches can be found for example in [1, 4, 5, 9, 16].

2.1. An overview of the theoretical results. Before coming to the finite element discretizations, we present a brief summary of theoretical results regarding mainly the existence of weak solutions, its uniqueness and regularity for Dirichlet boundary conditions. We restrict ourselves to steady flows, and we refer the interested reader to [11], section 5.1-5.4, where the evolutionary model with the space-periodic boundary conditions has been analyzed. The extension of the results to more realistic boundary conditions is in process.

We will use the standard notation: for $p \in [1, \infty]$, $k = 1, 2, \dots$, we denote $L^p(\Omega)$ and $W^{k,p}(\Omega)$ the Lebesgue and Sobolev spaces with the norms $\|\cdot\|_p$ and $\|\cdot\|_{k,p}$. By V_p we denote the closed subspace of functions from $W^{1,p}(\Omega)$ satisfying $\text{div } \vec{v} = 0$ in Ω and $\vec{v} = 0$ at $\partial\Omega$. The space of symmetric matrices of the type 2 by 2 is denoted by $\mathbf{R}_{\text{sym}}^{2,2}$.

The nonlinear tensorial function \mathbf{T}^E given by (2.3)–(2.4) is the typical example of a class of nonlinear potential tensorial functions \mathbf{T} 's satisfying the following assumptions

$$(2.5) \quad \exists \phi : \mathbf{R}_{\text{sym}}^{2,2} \mapsto \mathbf{R}_0^+ \quad \text{such that} \quad T_{ij}(\boldsymbol{\eta}) = \frac{\partial \phi(\boldsymbol{\eta})}{\partial \eta_{ij}} \quad \forall \boldsymbol{\eta} \in \mathbf{R}_{\text{sym}}^{2,2}$$

$$(2.6) \quad \exists c_1 > 0 : \quad \frac{\partial^2 \phi(\boldsymbol{\eta})}{\partial \eta_{ij} \partial \eta_{kl}} \xi_{ij} \xi_{kl} \geq c_1 (\varepsilon + |\boldsymbol{\eta}|)^{p-2} |\boldsymbol{\xi}|^2 \quad \forall \boldsymbol{\eta}, \boldsymbol{\xi} \in \mathbf{R}_{\text{sym}}^{2,2}$$

$$(2.7) \quad \exists c_2 > 0 : \quad \left| \frac{\partial^2 \phi(\boldsymbol{\eta})}{\partial \eta_{ij} \partial \eta_{kl}} \right| \leq c_2 (\varepsilon + |\boldsymbol{\eta}|)^{p-2} \quad \forall \boldsymbol{\eta} \in \mathbf{R}_{\text{sym}}^{2,2}$$

²Note that the assumption “the stress tensor at point \vec{x} depends on the velocity gradient through a general tensorial function”, can be reduced in 2 dimensions to the form (2.3) by the principle of the material frame indifference and by the representation of the isotropic tensors.

Consequently, see cf. [11], section 5.1, we also have

$$(2.8) \quad \exists c_3 > 0 : \quad T_{ij}(\boldsymbol{\eta})\eta_{ij} \geq c_3(|\boldsymbol{\eta}| - 1)^p \quad \forall \boldsymbol{\eta} \in \mathbf{R}_{\text{sym}}^{2,2}$$

$$(2.9) \quad \exists c_4 > 0 : \quad |\mathbf{T}(\boldsymbol{\eta})| \leq c_4(\varepsilon + |\boldsymbol{\eta}|)^{p-1} \quad \forall \boldsymbol{\eta} \in \mathbf{R}_{\text{sym}}^{2,2}$$

Let Ω be a smooth (C^2 - boundary) domain. Considering the Dirichlet boundary condition

$$(2.10) \quad \vec{v} = \vec{0} \quad \text{at} \quad \partial\Omega$$

we can define a weak solution to (2.1)–(2.2), (2.5)–(2.10).

Let $\vec{f} \in L^{p'}$, $p' = \frac{p}{p-1}$ and $\varrho(\vec{x}) = 1 \quad \forall \vec{x} \in \Omega$. A function $\vec{v} \in V_p$ is said to be a weak solution to our problem if

$$(2.11) \quad \int_{\Omega} v_j \frac{\partial v_i}{\partial x_j} \varphi_i d\vec{x} + \int_{\Omega} T_{ij}(\mathbf{D}(\vec{v})) D_{ij}(\vec{\varphi}) d\vec{x} = \int_{\Omega} f_i \varphi_i d\vec{x}$$

for all $\vec{\varphi}$ smooth with $\text{div } \vec{\varphi} = 0$.

Theorem 2.12. *Let $p > \frac{6}{5}$. Then there exists a weak solution to the problem (2.1)–(2.2), (2.5)–(2.10) which belongs to $W_{\text{loc}}^{2,p}(\Omega) \cap V_p$. If, in addition, $\|\vec{f}\|_{p'}$ is small enough then the solution is unique in the class of weak solutions from V_p .*

We are not aware of the fact that the result would have been formulated in this form before. In [10], the classical method of monotone operators provides the existence of the solutions for $p \geq \frac{3d}{d+2}$, where d denotes the dimension. Thus, if $d = 2$ we obtain the existence for $p \geq \frac{3}{2}$. In [3], the existence of weak solution were proved for $p \geq \frac{2d}{d+1}$, which in 2D gives the bound $p \geq \frac{4}{3}$. The method is based on the construction of a special L^∞ -test function and on strict monotonicity for \mathbf{T} , i.e.

$$(2.13) \quad (\mathbf{T}(\boldsymbol{\eta}) - \mathbf{T}(\boldsymbol{\xi})) \cdot (\boldsymbol{\eta} - \boldsymbol{\xi}) > 0 \quad \forall \boldsymbol{\eta}, \boldsymbol{\xi} \in \mathbf{R}_{\text{sym}}^{2,2}; \quad \boldsymbol{\eta} \neq \boldsymbol{\xi}.$$

In fact, the condition (2.6) implies a stronger kind of monotonicity than (2.13), namely

$$(2.14) \quad (\mathbf{T}(\boldsymbol{\eta}) - \mathbf{T}(\boldsymbol{\xi})) \cdot (\boldsymbol{\eta} - \boldsymbol{\xi}) \geq \frac{c_5 |\boldsymbol{\eta} - \boldsymbol{\xi}|^2}{\varepsilon + |\boldsymbol{\eta}|^{2-p} + |\boldsymbol{\xi}|^{2-p}} \quad \forall \boldsymbol{\eta}, \boldsymbol{\xi} \in \mathbf{R}_{\text{sym}}^{2,2},$$

valid also for $\varepsilon = 0$, see [11] for the proof of (2.14) for example.

In two dimensions, we can improve the last result using the special cancellation in the convective term when it is tested in the interior of the domain Ω by “ $\Delta \vec{v}$ ”, which in addition brings higher regularity for \vec{v} ($\vec{v} \in W_{\text{loc}}^{2,p}(\Omega)$) and consequently uniqueness for small $\|\vec{f}\|_{p'}$.

The proof of Theorem 2.12 can be deduced from the results of [7], where $C^{1,\alpha}$ -regularity (i.e. the Hölder continuity of gradients) has been proved locally (inside of Ω) for $p > \frac{6}{5}$ and globally (near the boundary) for $p > \frac{3}{2}$. It is possible to compare the results with [6] where this issue of “full” regularity has been successfully investigated for the space periodic problem even for $p > 1$.

2.2. Finite element discretization. First, we discretize the time variable t in the momentum equation (2.2) by some usual one θ -step scheme ($\theta = 1$ for backward Euler, $\theta = \frac{1}{2}$ for the Crank-Nicholson scheme) or by the fractional θ -step scheme

with 3 substeps each with different parameter θ . Given \bar{v}^n, p^n and time-step $k = t_{n+1} - t_n$, solve for unknown \bar{v}^{n+1}, p^{n+1}

$$(2.15) \quad \frac{\bar{v}^{n+1}}{k} + \theta[(\nabla \bar{v}^{n+1})\bar{v}^{n+1} - \operatorname{div}(\nu(\mathbf{D}(\bar{v}^{n+1}))\mathbf{D}(\bar{v}^{n+1}))] + \nabla p^{n+1} = \bar{g}$$

with the known right-hand side

$$\bar{g} = \frac{\bar{v}^n}{k} + \theta \bar{f}^{n+1} + (1 - \theta)\bar{f}^n - (1 - \theta)[(\nabla \bar{v}^n)\bar{v}^n - \operatorname{div}(\mu(\mathbf{D}(\bar{v}^n))\mathbf{D}(\bar{v}^n))]$$

Next, we introduce \mathbf{T}_h , a regular decomposition of the domain Ω into quadrilaterals and define the following spaces

$$(2.16) \quad L_h = \{q_h \in L^2(\Omega); q_h/T = \text{const.}, \forall T \in \mathbf{T}_h\},$$

$$(2.17) \quad S_h = \{v_h \in L^2(\Omega); v_h/T \in \tilde{Q}_1(T), \forall T \in \mathbf{T}_h, \\ F_\Gamma(v_h/T_1) = F_\Gamma(v_h/T_2) \text{ } \Gamma = T_1 \cap T_2, F_\Gamma(v_h) = 0, \forall \Gamma \subset \partial\Omega\},$$

where the nodal functional $F_\Gamma(v)$ can be chosen as (m_Γ is the midpoint of the edge Γ)

$$F_\Gamma(v) = |\Gamma|^{-1} \int_\Gamma v(\vec{x}) d\gamma \quad \text{or} \quad F_\Gamma(v) = v(m_\Gamma).$$

$\tilde{Q}_1(T)$ is a space generated by $\{x^2 - y^2, x, y, 1\}$ (so-called ‘‘rotated bilinear finite elements’’). For details see [15]. We apply usual spatial finite element discretization using weak formulation of equations (2.15) and spaces L_h for pressure and $\mathbf{H}_h = S_h^2$ for velocities to obtain a nonlinear algebraic system of following form.

$$(2.18) \quad [\theta_0 \mathbf{M} + \theta_1 k \mathbf{L}(\mathbf{u}) + \theta_2 k \mathbf{K}(\mathbf{u})] \mathbf{u} + k \mathbf{B} \mathbf{p} = \mathbf{f}$$

$$(2.19) \quad \mathbf{B}^T \mathbf{u} = 0$$

where \mathbf{u}, \mathbf{p} are the coefficient vectors corresponding to the approximation of \vec{u}, p in the spaces \mathbf{H}_h resp. L_h . The parameter θ_0 is set to 0 for the stationary case and 1 for the time-dependent case. Matrix \mathbf{M} corresponds to the mass matrix, \mathbf{K} corresponds to the non-linear convective term. The matrix \mathbf{L} in our case corresponds to the viscous term $\int_\Omega \mu(|\mathbf{D}(\vec{u})|^2) D_{ij}(\vec{u}) D_{ij}(\vec{\varphi}) d\vec{x}$.

We use two algorithms which can both be included in the general framework of the Multilevel Pressure Schur Complement (MPSC) methods developed in [19].

For the stationary problems we use the local MPSC variant. In this approach we deal with a coupled problem in \mathbf{u} and \mathbf{p} . First the nonlinear problem is linearized by outer fixed point iteration and the resulting linear problem is solved by a multigrid solver with the element-wise solution of small local Schur complement problems as a smoother and coarse grid solver (which in fact is very similar to the ‘‘Vanka smoother’’ (see [20]), but it can be generalized to be much more robust and efficient). This algorithm can be written as

$$(2.20) \quad \begin{bmatrix} \mathbf{u}^{m+1} \\ \mathbf{p}^{m+1} \end{bmatrix} = \begin{bmatrix} \mathbf{u}^m \\ \mathbf{p}^m \end{bmatrix} - \omega^m \sum_{T \in \mathbf{T}_h} \begin{bmatrix} \tilde{\mathbf{S}}_{/T} & k\mathbf{B}_{/T} \\ \mathbf{B}_{/T}^T & \mathbf{0} \end{bmatrix}^{-1} \left(\begin{bmatrix} \mathbf{S} & k\mathbf{B} \\ \mathbf{B}^T & \mathbf{0} \end{bmatrix} \begin{bmatrix} \mathbf{u}^m \\ \mathbf{p}^m \end{bmatrix} - \begin{bmatrix} \mathbf{g} \\ \mathbf{0} \end{bmatrix} \right)$$

where $\mathbf{S} = \theta_1 k \mathbf{L}(\mathbf{u}^m) + \theta_2 k \mathbf{K}(\mathbf{u}^m)$ and $\tilde{\mathbf{S}}$ can be a simplified version of \mathbf{S} , for example $\tilde{\mathbf{S}} = \operatorname{diag}(\mathbf{S})$. In practice, the applied preconditioner in (2.20) can be reduced to a one-dimensional problem with the FEM discretization used here.

For the time dependent problems we apply the global version of the MPSC method where by forming first the Schur complement problem we decouple the problem into a nonlinear equation for the velocity and the Poisson equation for pressure. This can be written as the following iterative scheme

$$(2.21) \quad \mathbf{p}^{m+1} = \mathbf{p}^m - \omega^m \mathbf{A}^{-1} (\mathbf{B}^T \mathbf{S}^{-1} \mathbf{B} \mathbf{p}^m - \frac{1}{k} \mathbf{B}^T \mathbf{S}^{-1} \mathbf{g})$$

where again \mathbf{S} has the same meaning as in previous paragraph and \mathbf{A} contains one or several easy invertible approximations of $\mathbf{B}^T \mathbf{S}^{-1} \mathbf{B}$. For solving the nonlinear problem for the velocity (i.e. inverting the matrix \mathbf{S}) we use again a fixed point iteration and multigrid method with successive over-relaxation smoother and coarse grid solver. The Poisson equation for the pressure is then solved (i.e. inversion of the matrix \mathbf{A}) with the multigrid solver. Again, this complete procedure can be used as a smoother in an outer multigrid such that the resulting numerical behavior of this algorithm is significantly better than the similar and well-known (single grid) variants of projection or fractional step algorithms (see [19]).

As regards the convergence of the solvers, we have found that generally the methods converge slower or do not converge at all as parameter α approaches 1, which might be expected because of the presence of higher gradients near the boundary and prescribed zero boundary condition (compare also with known theoretical results, section 2.1). The convergence is better for small or moderate Reynolds numbers ($\text{Re} = 10, 100$) when ε is close to 1 and almost does not depend on the value of α (in the range of values of $0.5 \leq \alpha \leq 1.0$). On the other hand, the convergence of the method does not depend on the value of ε for higher Reynolds number ($\text{Re} = 1000$).

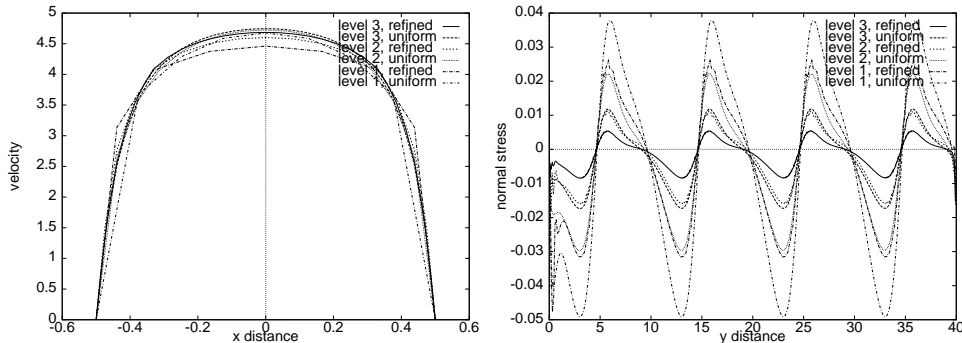


FIGURE 2. Velocity profiles at minimal clearance and normal extra stress on the wall of the channel for different grids. ($\text{Re} = 100$, $\alpha = 0.2$)

As regards the dependence of the obtained results on the refinement of the mesh, we concentrate on three quantities, the velocity \vec{v} , the pressure p and the stress \mathbf{T}^E . We start the construction of the mesh with a uniform grid with 2560 elements (referred to as level 1, uniform) and dividing each element into 4 elements by joining the midpoints of the opposite edges we obtain finer uniform grids (level 2 and 3, uniform). The second set of meshes is constructed from the grid with the same number of elements as the level 1, uniform, but refined toward the boundary (referred to as level 1, refined) and again by dividing each element into 4 elements

but this time in such a way that the new elements closer to the boundary are smaller we obtain another two grids (level 2 and 3, refined). While we do not observe any significant differences for the pressure we have found that the most sensitive quantity for the non-zero power-law index α is the velocity gradient near the wall and consequently the values of the stress tensor on the wall (see Fig. 2).

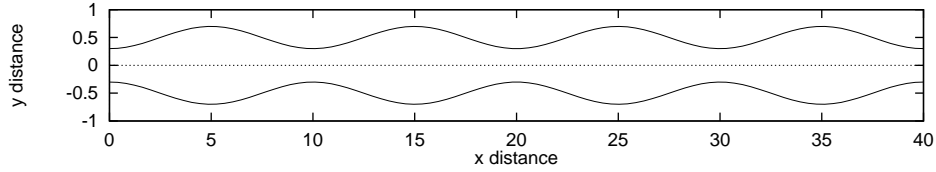


FIGURE 3. Dimensions of the domain.

Fluid	f0	f1	f2	f3	f4
α	0	0.25	0.5	0.5	1.0
ε	10^{-10}	10^{-10}	10^{-10}	1	1

a)

Channel	I	II	III
a	0.2	0.2	0.05
λ	10.0	2.5	2.5

b)

TABLE 1. The parameters of a) power-law model and b) channel oscillations.

3. NUMERICAL RESULTS FOR STATIONARY FLOW

We have made computations for all fluids mentioned in Table 1a): we will refer to f0 - f2 as the first set of fluids, while f3 - f4 form the second set. We have also varied the parameters of the domain (see fig. 3) namely the amplitude a and wavelength λ of the channel oscillations as shown in table 1b).

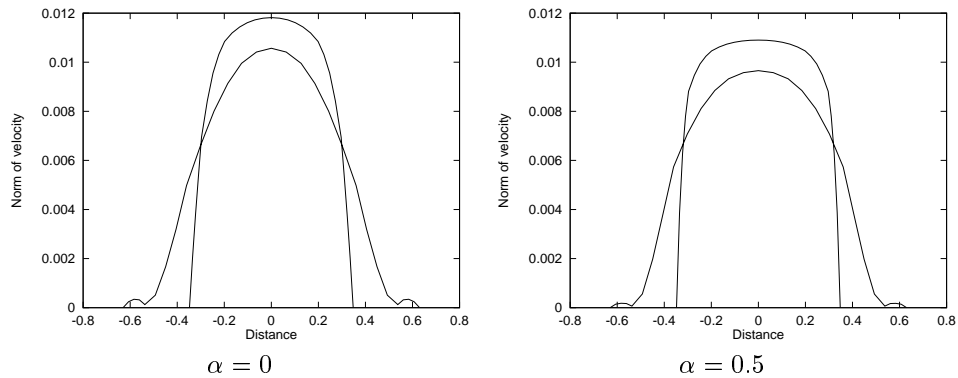


FIGURE 4. Velocity profiles at the maximal and minimal clearance.
Re = 100

3.1. Velocity profiles. The velocity profiles for different fluids and Reynolds numbers were computed. In Figure 4 we plotted the velocity profiles for channel II where the eddies forming secondary flow³ occurred near the boundary at the location of maximal clearance. As expected, the maximum of the velocity profile is at the center of the channel and it is higher in the narrow region than the maximum in wide region. With increasing the power-law exponent the maximum of velocity decreases and the velocity profile becomes more flatten. This decrease in the maximum of velocity is bigger at the location of maximal clearance. It can be noticed that we get very high values of the velocity gradient near the wall of the channel in the location of minimal clearance as the power-law exponent increases, as expected.

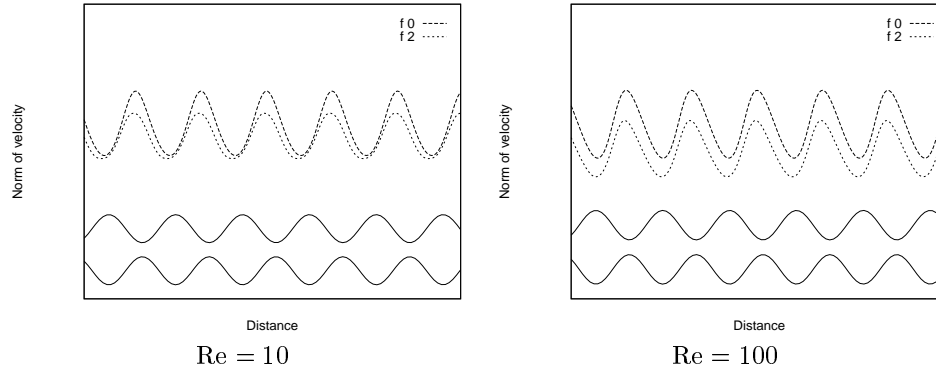


FIGURE 5. Centerline velocity. (The solid curve represents the channel.)

3.2. Centerline velocity. The norm of the velocity on the central axis of the channel II for different Reynolds numbers and different fluids are plotted in Figure 5. The solid curves represent the orientation of the channel sides. As expected, the velocity increases in the converging regions of the channel and decreases in the diverging regions. The length of accelerating region is shorter than the length of decelerating region. For low Reynolds number it can be observed that the maximum and the minimum of the centerline velocity do not exactly correspond to the point of minimal and maximal clearance of the channel. With increase in power-law exponent the maximum of velocity decreases, the minimum of velocity decreases for high Reynolds number but for low Reynolds number this decrease is much smaller.

3.3. Friction factor and Normal stress. The friction factor is defined by

$$f = \frac{\overline{T}_{12}}{\frac{1}{2}\rho U^2},$$

where \overline{T}_{12} is average shear stress on the wall of the channel.

For all cases the friction factor decreases with increasing Reynolds number. For the first set, the friction factor is higher for the fluid with the higher power-law exponent for low Reynolds number while for high Reynolds number the friction factor is lower for the fluid with the higher power-law exponent. The point of

³In non-Newtonian fluid mechanics, secondary flow is usually ment as minor flow caused by normal stress differences. In our case, the eddies forming secondary flow are due to geometry.

cross-over takes place for channels I and II (channels with different wavelength and same amplitude) at the same value of $Re = 40$ but for channel III the cross-over takes place at $Re = 60$. For the second set of fluids, we can observe the same behavior for high Reynolds number but in low Reynolds number the friction factor becomes nearly the same for all fluids.

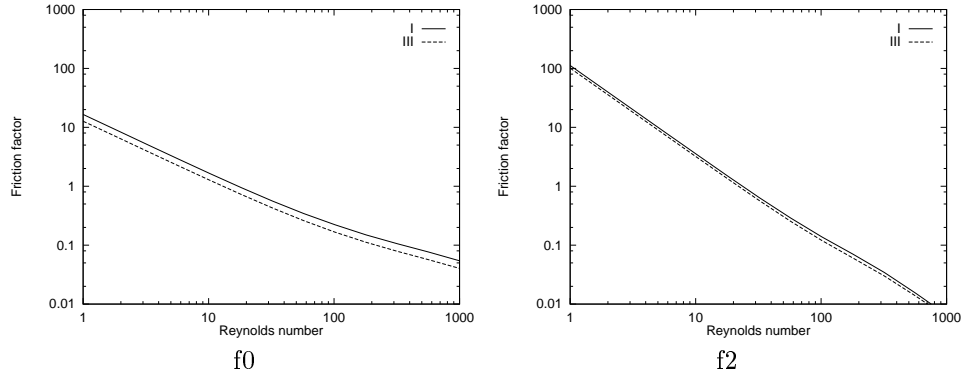


FIGURE 6. Friction factor vs Reynolds number for channels with the same aspect ratio.

In Figure 6 we can compare the friction factors for the channel I and the channel III. These two channels have the same aspect ratio $\frac{a}{\lambda}$. In this case, we can see that decrease in the friction factor is smaller for fluid with $\alpha = 0.5$ than for Newtonian fluid ($\alpha = 0$).

More importantly, at low Reynolds number the friction factor for the Newtonian case is lower than that for shear thinning fluid while the opposite is true at large Reynolds numbers. This is to be expected as the fluid shear thins and at the higher shear rates associated with large Reynolds number, the apparent viscosity is lower than the Newtonian viscosity.

In order to determine the amplitude of the normal stress we compute mean normal stress as a linear interpolation of the obtained values of the normal stress on the wall of channel. Then we subtract from the obtained values of the normal stress the mean normal stress and we compute an average of all local extremes and we get the amplitude of normal stress. We used non-dimensional form of the amplitude of the normal stress as suggested in [21]

$$(T_{22})_{\text{amp}}^* = \frac{2\rho\pi h^2}{3\lambda\mu_0^2 a} (T_{22})_{\text{amp}}.$$

We observe that the amplitude of the dimension-less normal stress increases with increasing Reynolds number except in a small range of Reynolds numbers ($0 < Re < 5$) in channel II. In all channels, for low Reynolds numbers ($Re < 1$ for channel I and III, $Re < 6$ for channel II) the amplitude of the dimension-less normal stress is higher for higher power-law exponent. For higher Reynolds numbers the amplitude of the dimension-less normal stress is again higher for fluid with higher power-law exponent. For channel II and Reynolds number greater than 600, the opposite behavior occurs. In this case, it is probably connected with occurrence of the secondary flow in the channel II.

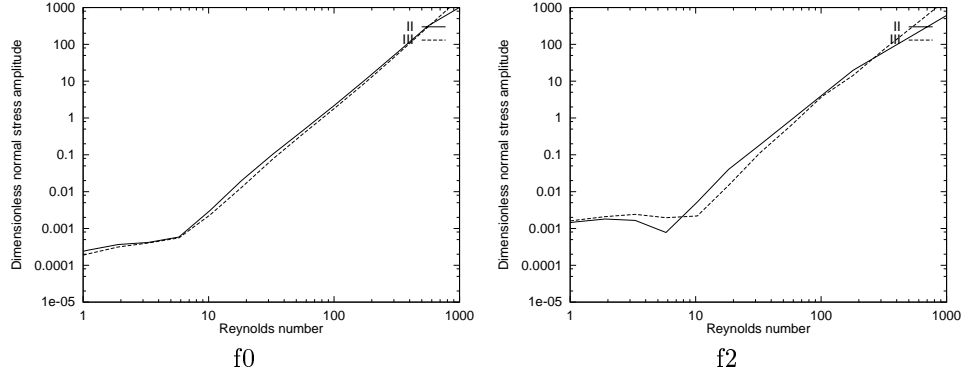


FIGURE 7. Normal stress amplitude vs. Reynolds number for channels with different amplitude a .

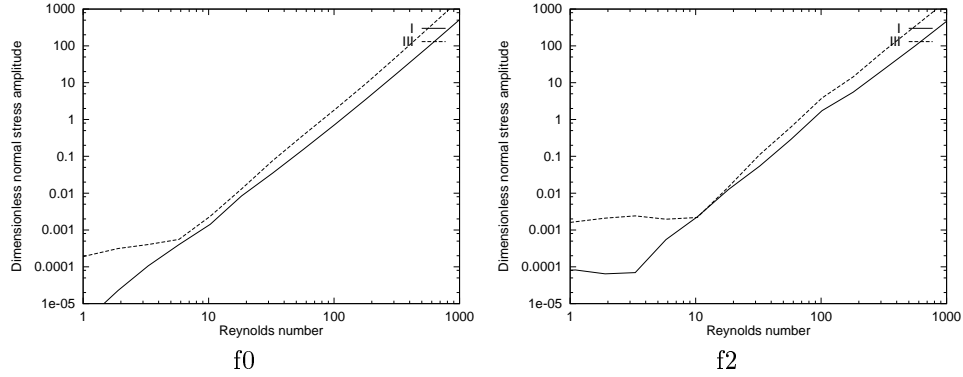


FIGURE 8. Normal stress amplitude vs. Reynolds number for channels with the same aspect ratio $\frac{a}{\lambda}$.

In Figure 7 we can compare the influence of the channel amplitude on the stress amplitude. It can be noticed that for the fluids with $\alpha = 0$ the stress amplitude is higher for the channel II ($a = 0.22$) than the stress amplitude for the channel III ($a = 0.05$) until $Re = 500$ after which the results are reversed. In the case of fluids with $\alpha = 0.5$ we observe that the normal stress amplitudes corresponding to different channel amplitudes have no clear ordering with the stress amplitudes switching roles as for which is larger, based on the range of the Reynolds number. Even the few calculations carried out clearly indicate that no correlation can be drawn with the changes in the stress amplitude with the wavelength.

In Figure 8 we compare the normal stress amplitude for the channels I and III for the first set of fluids. These two channels have the same aspect ratio $\frac{a}{\lambda}$. We notice the starting result, also collaborated by the experiments of R. C. Yalamanchili [21], that the normal stress amplitudes are different, at the same Reynolds number for the same aspect ratio thereby cautioning us against the use of the aspect ratio as a non-dimensional number with a view towards comparison.

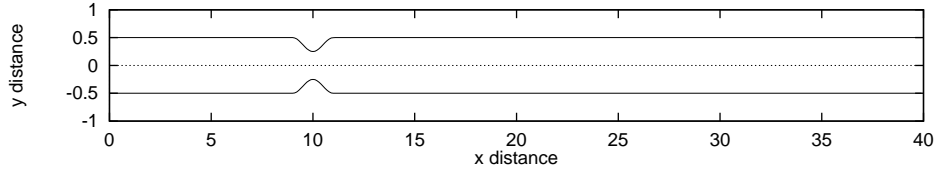


FIGURE 9. The dimensions of the domain.

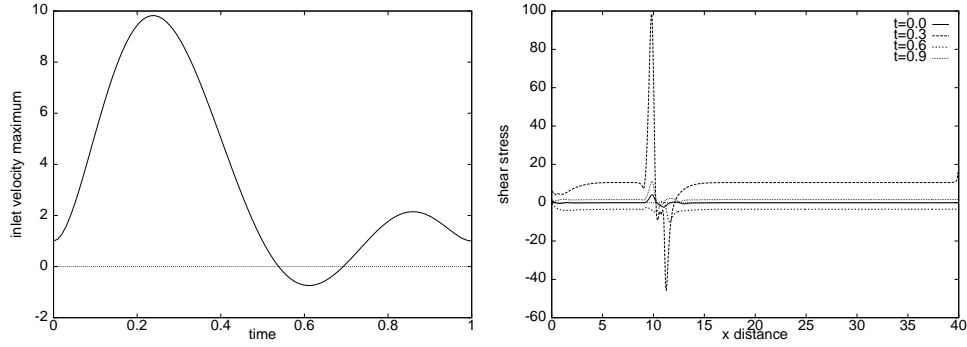
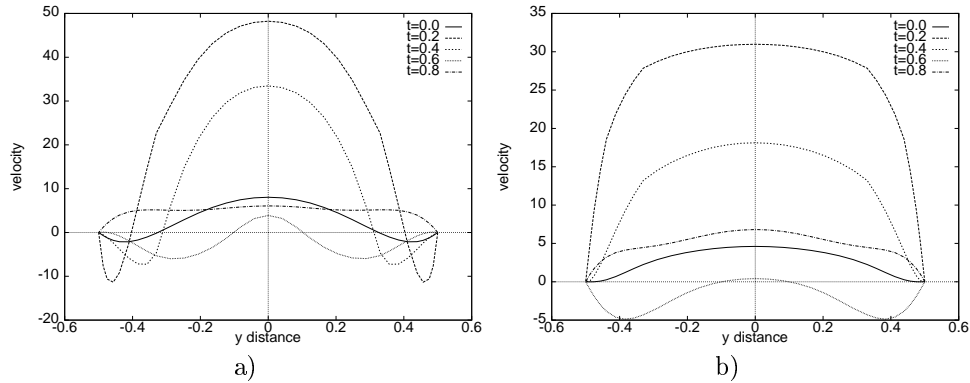


FIGURE 10. Maximum velocity at the inlet during one time period and wall shear stress at several time instants.

FIGURE 11. Velocity profiles for several time instants at a) $x = 11$ and b) $x = 30$.

4. PULSATILE FLOW

The time dependent calculations were done for two-dimensional flow in a channel with a symmetric constriction (see Fig. 9) and the fluid with the power-law index $\alpha = 0.2$. A similar axisymmetric channel is used in [17, 4] as a model for an artery with stenosis. We also take similar time-dependent inflow velocity which is parabolic with maximum value changing in time as shown in Fig. 10.

The Fig. 10 shows the shear stress on the wall of the channel at several time instants. The values vary sharply with x distance in the area of the stenosis and also in time during the period of the inflow velocity. It reaches the maximal value slightly before the narrowest point and at the same time as maximum of inflow

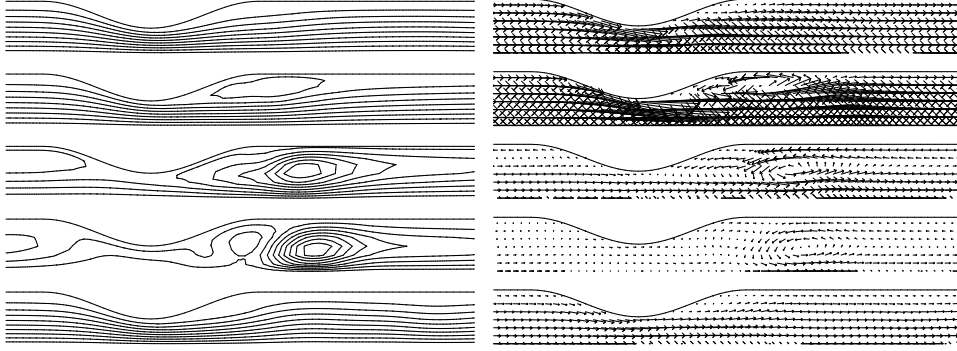


FIGURE 12. Instantaneous streamlines during one period for $t=0.1, 0.3, 0.5, 0.7, 0.9$. ($\alpha = 0.2$)

velocity occurs. The minimum value is reached behind the stenosis at the same time. In the rest of the domain the wall shear stress has positive value when the fluid flows in positive x direction and is negative when the direction of the flow is reversed.

Velocity profiles at locations behind the stenosis ($x = 11$) and further downstream ($x = 30$) are shown in Fig. 11. The whole flow pattern is shown in Fig. 12 as instantaneous streamlines and velocity vector plots at four different times. We can observe the forming of a secondary flow behind the stenosis as the inflow velocity grows. The eddy becomes larger and moves toward the center of the channel as the inflow velocity decreases. When the inflow velocity reverses the direction the flow starts to develop a second eddy there. In the second velocity pulse both eddies disappear.

5. CONCLUSION

In this paper, two numerical experiments were performed. First, we compared our results of the first stationary problem with the results of measurements done by R. C. Yalamanchili in [21]. Clearly, while the fluid tested by R. C. Yalamanchili is not a shear thinning fluid, it is nonetheless interesting that the predictions of our work show similar qualitative features as the experiments of R. C. Yalamanchilli. For the centerline velocity also we observed results similar to those found by Yalamanchili: 1) The maximum velocity occurs at the same location irrespective of the Reynolds number. 2) The increase in the Reynolds number causes the amplitude of the centerline velocity to increase, with no significant change in the wavelength. 3) The maximum velocity in the converging region of the channel is reached in a shorter distance, when compared to the distance in which the minimum of velocity is reached in the diverging region. For the velocity profiles we observed similar eddies forming secondary flow in the channel with smaller wavelength and bigger amplitude (see Fig. 4 and Fig. 13). For the friction factor we did not observe completely different characteristics for the channels with the same aspect ratio. For the amplitude of the dimension-less normal stress we observed: 1) An increase in channel wavelength decreases the amplitude of the normal stress. 2) An increase in channel amplitude can increase or decrease the amplitude of the normal stress depending on the Reynolds number. Which implies that the aspect ratio $\frac{a}{\lambda}$ is not a

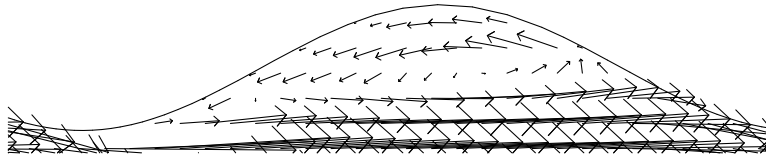


FIGURE 13. An eddy forming secondary flow in channel II.

good characteristic number for this case of channel where the width of the channel and wavelength and amplitude of the wall corrugation are comparable. All in all, we found that our numerical simulations predict results that are qualitatively in keeping with the experimental results of R. C. Yalamanchili et. al.

In the second part we have tested the solver in time-dependent problem with periodically varying inflow velocity. Concerning the wall shear stress we have observed dramatic variation of its value in the region of the stenosis in time and in distance x . The velocity field structure showed the presence of secondary flow behind the constriction and significant backward flow near the walls when the inflow velocity was in negative x direction. Our results exhibit good correspondence with extensive results presented in [17]. Despite the fact that their results were computed for axially symmetric tube while ours are obtained for 2-dimensional channel the qualitative behavior of the wall shear stress and the flow pattern is similar.

These tests show that the new solver for simulating flows of the power-law fluids, presented in this paper, works in a reasonably efficient way for our problem in a certain range of parameters and is suitable for further development for more complex problems in blood rheology. More information about the numerical tools and the code itself can be found under <http://www.featflow.de>.

REFERENCES

- [1] Böhme, G., Rubart, L.: Non-Newtonian flow analysis by finite elements, *Fluid Dynamics Research* 5, 147–158, 1989.
- [2] Čadek, O., Martinec, Z., Matyska, C.: Spectral variational approach to the non-Newtonian Stokes problem in a spherical shell, *Computer Physics Communications* 71, 56–70, 1992.
- [3] Frehse, J., Málek, J., Steinhauer, M.: An existence result for fluids with shear dependent viscosity - steady flows, *Nonlinear Analysis, Theory Meth. Appl.* 30, 3041–3049, 1997.
- [4] Despotis, G. K., Tsangaris, S.: A Fractional Step Method for Unsteady Incompressible Flows on Unstructured Meshes, *Int. J. of Comp. Fluid Dynamics* 8, 11–29, 1997.
- [5] Du, Q., Gunzburger, M.D.: Finite-element approximations of a Ladyzhenskaya model for stationary incompressible viscous flow, *SIAM J. Numer. Anal.*, Vol. 27, No. 1, 1–19, 1990.
- [6] Kaplický, P., Málek, J., Stará, J.: Full regularity of weak solution to a class of nonlinear fluids in two dimensions - stationary periodic problem, *Comment. Mat. Univ. Carol.* 38 (No. 4), 681–695, 1997.
- [7] Kaplický, P., Málek, J., Stará, J.: $C^{1,\alpha}$ -regularity of weak solutions to a class of nonlinear fluids in two dimensions – stationary Dirichlet problem, *Zap. Nauchn. Sem. POMI* 259 (No.29), 89–121, 1999.
- [8] Kjartanson, B.H., Shields, D.H., Domaschuk, L., Man, C.S.: The creep of ice measured with the pressure-meter, *Can. Geotech. J.*, 25, 250–261, 1988.
- [9] Legat, V., Oden, J.T.: An adaptive hp-finite element method for incompressible free surface flows of generalized Newtonian fluids, *Z. Angew. Math. Phys.* 46, 643–678, 1995.
- [10] Lions, J.L.: *Quelques méthodes de résolution des problèmes aux limites non linéaires*, Dunod, Paris, 1969.
- [11] Málek, J., Nečas, J., Rokyta, M., Růžička, M.: *Weak and measure-valued solutions to evolutionary PDE's*, Chapman & Hall, London, 1996.

- [12] Malevsky, A.V., Yuen, D.A.: Strongly chaotic non-Newtonian mantle convection in the Earth's mantle, *Geophys. Astrophys. Fluid Dyn.*, 65, 149–171, 1992.
- [13] Mansutti, D., Rajagopal, K. R.: Flow of a shear thinning fluid between intersecting planes, *International Journal of Non-Linear Mechanics*, 26, 769–775, 1991.
- [14] Rajagopal, K. R.: Boundary layers in non-linear fluids, in book *Trends in applications of mathematics to mechanics* (eds MDP Monteivo Marques and J. F. Rodrigues), Pitman Monographs and Surveys in Pure and Applied Mechanics, Longman 77, 209–218, 1995.
- [15] Rannacher, R., Turek, S.: A simple non-conforming quadrilateral Stokes element, *Numer. Meth. Part. Diff. Eqn.*, 8, 97–111, 1992.
- [16] Rubart, L., Böhme, G.: Numerical Simulation of shear-thinning flow problems in mixing vessels, *Theoret. Comput. Fluid Dynamics* 3, 95–115, 1991.
- [17] Tu, C., Deville, M.: Pulsatile Flow of Non-Newtonian Fluids through Arterial Stenosis, *J. Biomechanics*, vol. 29, 889–908, 1996.
- [18] Turek, S.: FEATFLOW. Finite element software for the incompressible Navier-Stokes equations: User Manual, Release 1.1, Technical report, 1998.
- [19] Turek, S.: Efficient solvers for incompressible flow problems: An algorithmic and computational approach, *LNCS 6*, Springer-Berlin, 1998.
- [20] Vanka, S.P.: Implicit multigrid solutions of Navier-Stokes equations in primitive variables, *J. Comp. Phys.*, 65, 138–158, 1985.
- [21] Yalamanchili, R.C.: Flow of non-Newtonian fluids in corrugated channels, *Int. J. Non-Linear Mechanics*, Vol. 28, No. 5, 535–548, 1993.
- [22] Yalamanchili, R.C., Sirivat, A., Rajagopal, K.R.: An experimental investigation of the flow of dilute polymer solutions through corrugated channels, *J. Non-Newtonian Fluid Mech.* 58, 243–277, 1995.
- [23] Yeleswarapu, K.K., Antaki, J.F., Kameneva, M.V., Rajagopal, K.R.: A generalized Oldroyd-B model as constitutive equation for blood, *Proceedings of the Second World Congress of Biomechanics*, 1994.

(J. Hron and J. Malek) MATHEMATICAL INSTITUTE OF CHARLES UNIVERSITY, SOKOLOVSKÁ 83, 186 75 PRAGUE 8, CZECH REPUBLIC

(S. Turek) INSTITUTE FOR APPLIED MATHEMATICS, UNIVERSITY OF DORTMUND, VOGELPOTHSWEG 87, 44227 DORTMUND, GERMANY